Convectively generated gravity waves simulated by NAM-SCA

Jun-Ichi Yano, Todd P. Lane

AGU PUBLICATIONS

JGR

Journal of Geophysical Research: Atmospheres

RESEARCH ARTICLE

10.1002/2013JD021419

Key Points:
- Representation of convection-generated gravity waves
- Nonhydrostatic anelastic model with segmentally constant approximation
- NAM-SCA works for this purpose under a strong compression rate even down to 0.1

Correspondence to:
J.-I. Yano,
j.yano@reading.ac.uk

Citation:
Yano, J.-I., and T. P. Lane (2014), Convectively generated gravity waves simulated by NAM-SCA, *J. Geophys. Res. Atmos.*, *119*, 9267–9289, doi:10.1002/2013JD021419.

Received 23 DEC 2013
Accepted 1 MAY 2014
Accepted article online 6 MAY 2014
Published online 6 AUG 2014

Convectively generated gravity waves simulated by NAM-SCA

Jun-Ichi Yano[1] and Todd P. Lane[2]

[1]GAME/CNRS, CNRS-INSU-Météo France, Toulouse, France, [2]School of Earth Sciences and ARC Centre of Excellence for Climate System Science, University of Melbourne, Melbourne, Victoria, Australia

Abstract Convectively generated gravity waves are an unresolved process in global models. However, parameterization of their effects is difficult because the parameterized wave spectrum must be linked to the convective source, which is itself parameterized. Here we use the NAM-SCA model (nonhydrostatic anelastic model with segmentally constant approximation), which is midway between a cloud-resolving model and convection parameterization. Unlike conventional convection parameterizations, NAM-SCA is built directly upon a nonhydrostatic anelastic model, and thus it describes dynamical processes consistently but in a "compressed" manner (i.e., with truncation via a spatiotemporal adaptive mesh) that facilitates its potential use as a parameterization. As a result, under the dynamical framework of NAM-SCA, convection generates a spectrum of gravity waves in a physically consistent manner without any additional assumptions or simplifications. The present study examines the capacity of NAM-SCA for generating gravity waves from convection under varying degree of "compression" and assesses its viability as a physically consistent convective gravity wave source parameterization. By taking the TWP-ICE (Tropical Warm Pool-International Cloud Experiment) period for the case study, NAM-SCA successfully represents the convectively generated gravity waves even down to the compression rate of 0.1. Analysis in the wave number frequency space shows that the compression behaves as a weak low-pass filter in wave number, but higher-frequency components generated by dynamic adaptation partially compensate the filtering effect making the net Reynolds stress relatively insensitive to compression.

1. Introduction

The importance of convectively generated gravity waves in various atmospheric processes, especially those in the stratosphere and mesosphere, is widely recognized [*Fritts and Alexander*, 2003]. Numerous modeling studies [*Fovell et al.*, 1992; *Holton and Alexander*, 1999; *Piani et al.*, 2000; *Lane et al.*, 2001; *Beres et al.*, 2002; *Song et al.*, 2003] have already been performed on the generation of gravity waves by tropical deep moist convection. The need for parameterization of convectively generated gravity waves is well established, along with other orographic and nonorographic sources. Parameterizations of convective gravity waves have undergone substantial development in recent years [*Beres et al.*, 2005; *Song and Chun*, 2005; *Song et al.*, 2007; *Eckermann et al.*, 2009], making them arguably more advanced than parameterizations of other nonorographic sources (e.g., fronts). However, in comparison to other processes (e.g., convection, turbulence, etc.) the parameterization of the convective gravity wave source is still in its relative infancy.

The complete parameterization of convectively generated waves relies on two distinct components: (1) the source spectrum of the gravity waves and (2) the wave dispersion and dissipation (viz., wave drag). The second component is more general and commonly used for all nonorographic sources [e.g., *Alexander and Dunkerton*, 1999; *Warner and McIntyre*, 2001], relying on a specification of the source spectrum, which can be fixed in time (viz., a background spectrum) or with spatiotemporal variations as per a physical source parameterization. Recent attempts at parameterizing the source of convective gravity waves have used linear theory to determine the spectrum of gravity waves generated by diabatic heat sources [*Beres et al.*, 2002; *Song and Chun*, 2005]. However, despite being a major step forward, these methods require assumptions about the spatial and temporal structure of the heat source, which are not necessarily consistent with the assumptions within the associated convection parameterization. A major challenge is linking these parameterized processes in a physically consistent way. One option to parameterize convective gravity waves is to build a source parameterization as a direct extension of the parent convection parameterization. However, a major difficulty in this approach is that gravity waves cannot be readily represented by a simple extension of the existing mass flux formulation, which is used in most of current convection parameterizations. A more general approach is required.

Yano et al. [2005] proposed the mode decomposition as a general approach for developing a representation of subgrid-scale physical processes. Specifically, *Yano et al.* [2010], *Yano and Bouniol* [2010], and *Yano and Baizig* [2012] developed the nonhydrostatic anelastic model with segmentally constant approximation (NAM-SCA), which contains a number of simplifications (e.g., simple microphysics and two-dimensional dynamics) and a spatially and temporally adaptive mesh that makes it computationally efficient (or "compressed"). Despite the simplifications, NAM-SCA has been shown to provide a reasonable representation of convective processes [*Yano and Bouniol*, 2010; *Yano et al.*, 2012a]. Moreover, although NAM-SCA was originally developed for simulating convective processes, it can, by design, represent any subgrid-scale physical processes, including convectively generated gravity waves. NAM-SCA simplifies the cloud-resolving model (CRM) through compression but retains the capability to study the dynamics of convective gravity waves and their relationships to convection.

One application of NAM-SCA is that it can be used as an efficient "superparameterization" (originally proposed by *Grabowski and Smolarkiewicz* [1999]; see also *Randall et al.* [2003]). (The concept of superparameterization is that a two-dimensional cloud-resolving model (CRM) is embedded within each grid cell of a global "parent" model to replace the convection parameterization.) The biggest challenge of the existing superparameterization approach is that it is prohibitively computationally expensive. The advantage of NAM-SCA is that, because of its compression, it is much less computationally expensive than a regular CRM. Thus, a superparameterization using NAM-SCA could be more feasible.

In their superparameterization implementation *Khairoutdinov et al.* [2008] removed all of the regular subgrid-scale parameterizations from the host global model (and replaced them with CRMs), except for the gravity wave parameterization. Those CRMs did not, however, provide information to the wave drag parameterization. However, the CRMs within the superparameterization could actually be utilized to provide a more realistic (and physically consistent) spectrum of convectively generated gravity waves. Here we advocate the potential for extending the superparameterization approach such that the subgrid CRMs act as a convectively generated gravity wave source parameterization that could be linked directly to the wave drag parameterization of the parent global model.

The main aim of this paper is to explore the potential for NAM-SCA to be embedded into a larger-scale model as a unified parameterization of convection and convectively generated gravity waves. The main advantage of such an approach is that artificial assumptions about the waves and their relationship to convection are avoided, because the waves are generated in an internally consistent manner. Although the current version of NAM-SCA is not advanced in its treatment of cloud processes (e.g., it lacks ice microphysics), its ability to link the gravity wave source spectrum directly to the convective processes is a significant advantage compared to existing approaches.

A full application of NAM-SCA as a unified convection and gravity wave source parameterization requires extensive development and testing. The present preliminary study is simply a prototype parameterization for convectively generated gravity waves. Our focus is on parameterizing the source of the waves (and not the wave dissipation and wave drag). We consider two issues in this paper. First, and most importantly, we examine the influence of the truncation of NAM-SCA on the spectrum of gravity waves in order to assess the advantages of NAM-SCA over a full-CRM superparameterization. Second, we examine the effects of the upper boundary conditions and their effects on the spectrum of stratospheric waves (and their possible artificial reflections) in this model framework.

The paper is arranged as follows. Section 2 presents background on the NAM-SCA approach. Section 3 describes the model setup. The model is then applied to a case study from the Tropical Warm Pool-International Cloud Experiment (TWP-ICE), as introduced in section 4. Section 5 presents examples of waves generated by convection in the model. The capacity of NAM-SCA for representing convectively generated gravity waves under varying degrees of compression is then examined, first with no background zonal wind in section 6 and then with the observed background zonal wind in section 7. The results and their implications for future investigations are summarized in section 8.

2. Background for NAM-SCA

NAM-SCA is an effort to close the gap between explicit modeling and parameterization [*Yano et al.*, 2005]. Its key inspiration is the multiresolution analysis based on wavelets [*Mallat*, 1998], which represents various

localized coherency in geophysical flows in a compressed manner with a limited number of wavelet modes. NAM-SCA pursues a similar idea through mode decomposition in physical space.

The NAM-SCA formulation has emerged from analyzing the basic structure of the mass flux formulation, which is commonly adopted in convection parameterizations. Mass flux parameterization can be considered as a decomposition of the grid box domain into a set of convective towers described by mass fluxes and a horizontally homogeneous surrounding environment, which can be interpreted as a mode decomposition in analogy with the multiresolution analysis. Thus, a conceptual link between mass flux and wavelets exists. In many ways, such a generalization of the mass flux formulation can be considered as a "compression" of a CRM or "compressed superparameterization" [*Yano et al.*, 2012a].

Geometrically, the mass flux decomposition is that of approximating the whole grid box by a set of constant segments, categorized as convective updraft, environment, etc. (segmentally constant approximation, SCA [*Yano*, 2012a]). Furthermore, the model formulation under SCA simply corresponds to a lowest-order finite-volume numerical algorithm [cf. *Godunov*, 1959; *LeVeque*, 2002]. Here SCA departs from the conventional finite-volume method by drastically truncating the number of finite volumes so that a single volume may describe a single convective updraft. The number of finite volumes may even be reduced to two when a prototype for bulk mass flux parameterization is considered [*Yano and Baizig*, 2012].

The above concepts form the basis of NAM-SCA, which is a new type of a time-dependent finite-volume adaptation method in analogy with wavelet compression. Details of a time-dependent adaptation procedure are found in *Yano et al.* [2010] with a short summary given in section 3.2. NAM-SCA is already implemented into two versions of single-column models for ECMWF (European Centre for Medium Range Weather Forecasts) Hamburg version Atmospheric Model and the Australian Community Climate and Earth-System Simulator [*Yano et al.*, 2012a]. The concept of NAM-SCA furthermore provides a link between parameterization and downscaling [*Yano*, 2010].

NAM-SCA is primarily designed to describe coherent localized structures in the atmospheric flows such as deep-convective towers efficiently. It is not designed to study nonlocalized structures such as gravity waves generated from deep convection. Nevertheless, *Yano and Baizig* [2012] have successfully simulated a transformation from a convective regime to a gravity wave regime with increasing Richardson numbers under the severest truncation. The present paper reports successful simulations of the generation of gravity waves from convective system by NAM-SCA under standard compression rates for the TWP-ICE period.

3. Model Setup

3.1. General Aspects

NAM-SCA is constructed from a standard CRM (NAM) but designed to work like a parameterizaion. Its current configuration is in two dimensions with the vertical velocity, w', the potential temperature, θ, and the three water components (water vapor, cloud water, and precipitating water) as prognostic variables. The zonal wind, u', is diagnosed from the vertical velocity by mass continuity. The prime notation indicates a deviation from the domain mean. The domain mean zonal wind, $\bar{u}$, is prescribed as an idealized profile or from observations. Assuming a periodic boundary condition, the domain-mean vertical velocity vanishes, although it is implicitly included as a part of large-scale forcing.

The formulation for NAM-SCA is presented in *Yano et al.* [2010] for a dry atmosphere. The adopted bulk cloud microphysics are described in *Yano and Bouniol* [2010, 2011]. The reference state for potential temperature and water vapor is defined by an observed initial sounding. These profiles are also used as initial conditions.

No explicit eddy diffusion is included in NAM-SCA. Both vertical and horizontal advections are calculated by an upstream scheme without adding extra numerical diffusion. The model has no horizontal derivatives other than the horizontal advection terms. As a result, in combination with a finite-volume formulation in the horizontal direction, the minimum mesh size, Δx (fixed to 2 km in the present study), is the actual minimum scale resolved in the model (with the minimum resolved wavelength $2\Delta x = 4$ km). This differs from conventional finite difference schemes where the effective minimum resolved wavelength is at least $6\Delta x$. The lack of eddy diffusion demands additional considerations for gravity wave simulations as discussed in section 3.3.

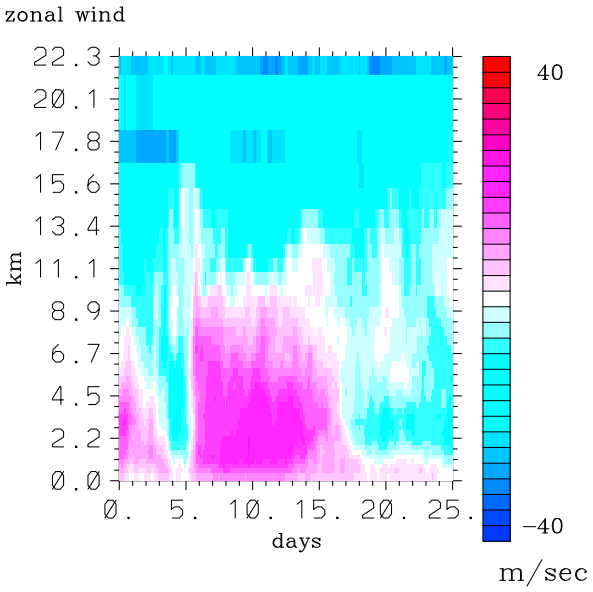

Figure 1. Time height section of the observed zonal wind during the TWP-ICE period starting on 20 January 2006.

We use NAM-SCA in a "stand-alone" single-column configuration as detailed in *Yano et al.* [2012a]: NAM-SCA is driven by the total "large-scale" advection tendencies for the potential temperature and the water-vapor mixing ratio provided every 3 h (cf. section 4). The radiative tendencies are calculated every 3 h using a radiation code from the National Center for Atmospheric Research Community Climate Model 2 (CCM2) [*Kiehl et al.*, 1994]. The cloud fraction for the radiation calculation is estimated within NAM-SCA with a definition of the cloud-water mixing ratio above 10^{-2} g/kg. The prescribed sensible and latent surface fluxes are provided by ECMWF (European Centre for Medium Weather Forecast) analysis for the TWP-ICE area (cf. section 4). Surface fluxes are assumed to decrease linearly with height and vanish at 500 m above ground.

We use a 512 km horizontal domain with the minimum horizontal mesh size of $\Delta x = 2$ km, as retained at the lower model layer, and $\Delta X = 256$ km as the largest possible model mesh size. A stretched vertical coordinate is used with the lowest layer depth $\Delta z_0 = 50$ m, and gradually stretched to $\Delta z_n = 41000$ m up to the model top level, $H = 70$ km, with the rigid-lid top boundary condition. The default model parameters are listed in the Appendix A.

3.2. Compression

NAM-SCA can compress the system by reducing the resolution where less detail is required with a time-dependent mesh adaptation procedure. A finite-volume interface is stretched vertically whenever a feature with a sharp contrast of physical values arises at a given finite-volume interface. For example, the finite volumes are stretched upward when a convective plume grows upward. Whenever a convective plume dissipates, the additional finite-volume interfaces are removed. This removal is undertaken by examining the change in a variable over a given finite-volume interface, and when it is small enough the two finite volumes merge. These conditions are examined for all five prognostic variables. The threshold for activation and deactivation of volume interfaces is defined relative to the standard deviation of each variable at a given vertical level. The relative threshold, γ, for activation and deactivation of finite-volume interfaces is kept the same for both activation (γ_a) and deactivation (γ_d: i.e., $\gamma \equiv \gamma_a = \gamma_d$).

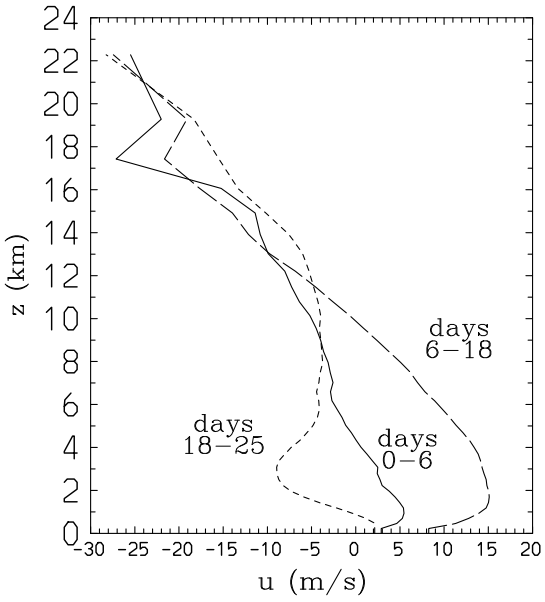

Figure 2. The zonal wind profiles averaged over the three subperiods during TWP-ICE: days 0–6 (solid curve), 6–18 (long-dash curve), and 18–25 (short-dash curve).

The key parameter, γ, for compression is called the *compression threshold*. We measure the *compression rate* of the model by the ratio of the total active volume segments to that for a full-resolution case, which is always presented in terms of average over the whole simulation period.

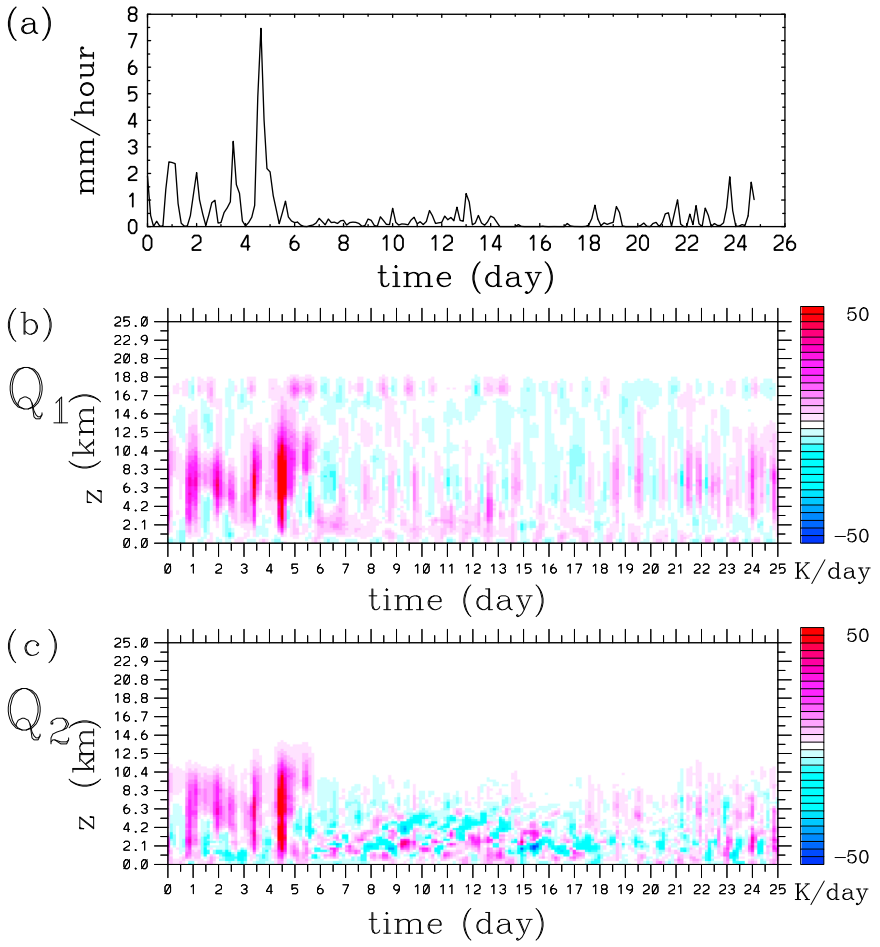

Figure 3. Observations during TWP-ICE starting on 20 January 2006: (a) precipitation time series, and the time height section of (b) apparent heat source, Q_1, and (c) apparent moisture sink, Q_2. The values are shown for the range of −50 K/day to 50 K/day by the tones of blue (lowest) to red (highest) with the white corresponding to the zero value.

Enhanced compression (a lower compression rate) is achieved at a high compression threshold, γ. The enhanced compression accelerates the model computations. Full details of the compression procedure are given in *Yano et al.* [2010].

3.3. Sponge Layer

In order to prevent artificial reflection of the gravity waves from the rigid top, a sponge layer is added to an upper part of the model, in which all the prognostic variables are damped to the reference values. The prescribed damping rate, λ_R, linearly increases from the bottom, $z_{1,R} = 25$ km, of the sponge layer to a height, $z_{2,R} = 60$ km (with $z_{2,R} = 45$ km as a possible alternative) above which the maximum value $\lambda_R = 1/\tau_R$ is used with the damping time scale, $\tau_R = 60$ s.

The parameter values are chosen by the following considerations: the sponge layer must be high enough so that the absorption effects as well as partial reflections are not seen over a vertical range of our interests. It also must be thick enough so that all the upward propagating gravity waves are sufficiently damped before reaching the rigid-lid top.

Due to a total absence of numerical diffusion, in spite of its overall stability, the model generates numerical modes, in particular, a deep horizontally fast propagating mode that extends over the whole vertical depth of the model domain. The deep mode is more likely generated when a shorter time step is taken; however, for numerical stability of the computation as a whole, a sufficiently short time step is required. For the present case study, the time step, $\Delta t = 5$ s, is the maximum for guaranteed stability, although these runs are still relatively noisy. A further reduction of the time step to $\Delta t = 2$ s induces the

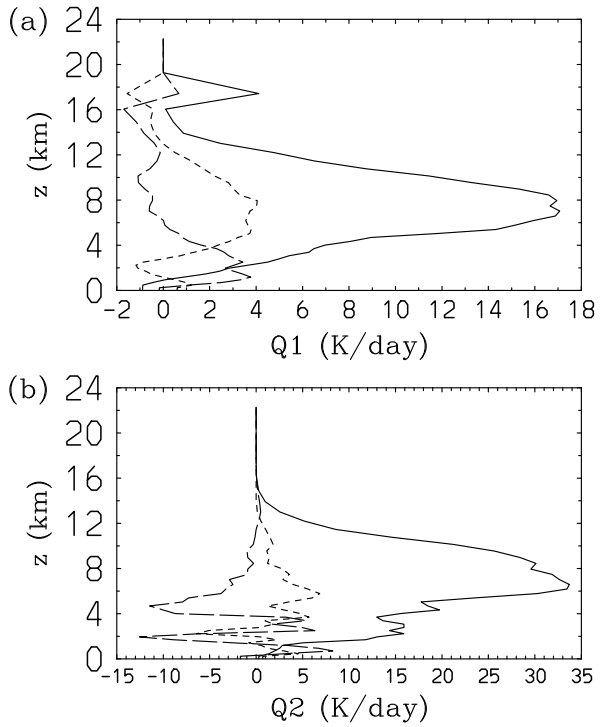

Figure 4. The same as Figure 2 for the three subperiods during TWP-ICE (shown in Figure 2) but for (a) apparent heat source, Q_1, and (b) apparent moisture sink, Q_2.

numerically unstable deep modes with a modest sponge layer with $\tau_R \geq 120$ s. To solve the latter problem, relatively strong damping is required in the sponge layer. Taking these issues into account, we finally set $\tau_R = 60$ s and $\Delta t = 2$ s. Note that these settings and limitations are specific to NAM-SCA and do not necessarily correspond to the requirements of a more traditional CRM.

4. TWP-ICE: Background State

We take a period of 25 days from 20 January to 13 February 2006 during TWP-ICE, which was an experiment centered over Darwin, Australia, and the adjoining Tiwi Islands [*May et al.*, 2008]. The study area is situated at the south edge of the Warm Pool in the Western Pacific but is also strongly influenced by land forcing from both the Australian continent and Tiwi Islands. Strong land forcing leads to vigorous convection that sometimes penetrates the lower stratosphere and generates relatively large-amplitude gravity waves. Storms generated over Tiwi Islands are so vigorous that they are called *Hectors* [*Crook*, 2001] and have been commonly studied in the context of convectively generated gravity waves [*Lane et al.*, 2001; *Lane and Reeder*, 2001; *Piani et al.*, 2000; *Hankinson et al.*, 2014a, 2014b].

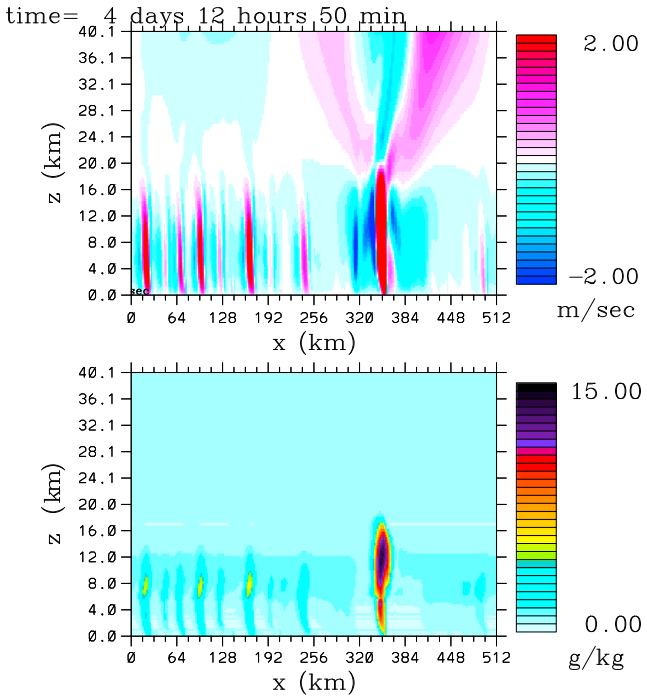

Figure 5. An example of simulated convectively generated gravity waves by a full-resolution version of NAM-SCA. Here the case with $z_{2,R} = 60$ km with $\tau_R = 60$ s is shown: (top) the vertical velocity and (bottom) the total condensate at 4 days 12 h 50 min of the simulation.

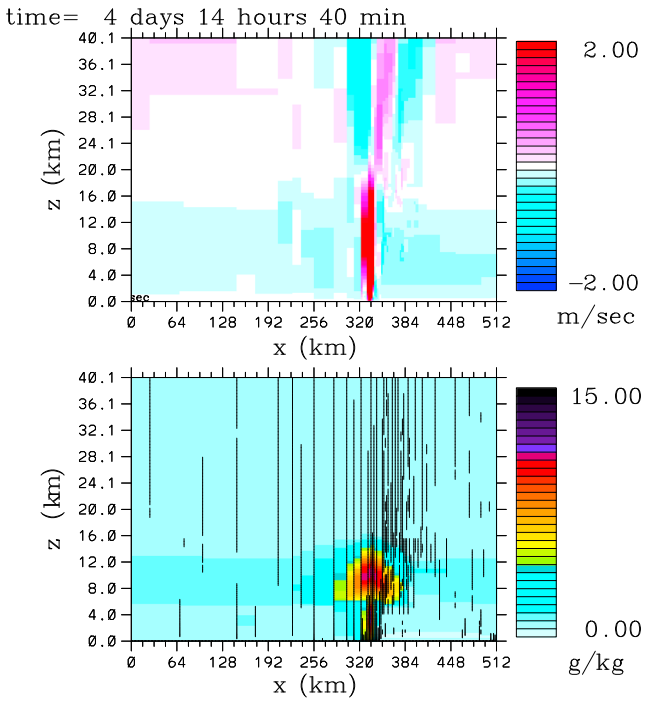

Figure 6. An example of simulated convectively generated gravity waves by NAM-SCA with the standard compression ($\gamma = 1$). The other parameters are the same as in Figure 5: (top) the vertical velocity and (bottom) the total condensate at 4 days 14 h 40 min of the simulation. Figure 6 (bottom) also shows distribution of finite-volume segments by indicating their boundaries with vertical solid lines.

Vertical propagation of gravity waves is significantly influenced by the vertical profile of the zonal wind; its time height section is shown in Figure 1 along with the vertical profiles for three subperiods (Figure 2). The first 5 days are characterized by an easterly wind shear (solid curve, Figure 2); as seen by a precipitation time series (Figure 3a), this corresponds to the most convectively active period. A period with a deep westerly wind occurs between days 6 and 18 (long-dashed curve, Figure 2). Though such a deep westerly is characteristic of an active phase of monsoon [cf. *Drosdowsky*, 1996], the precipitation for this period is relatively weak. Finally, the last 7 days corresponds to a break period characterized by easterly winds (short-dashed curve, Figure 2).

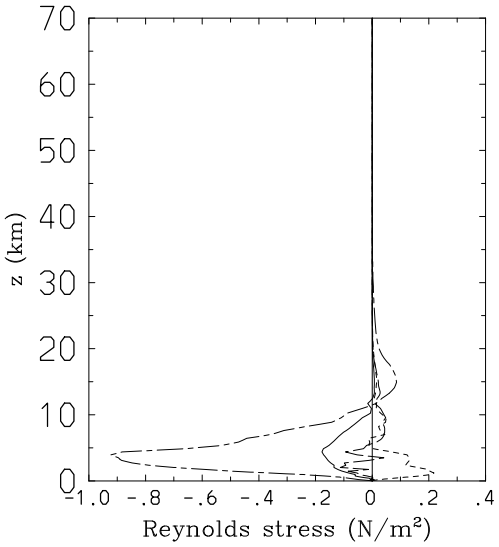

Figure 7. The vertical profiles of the domain-averaged Reynolds stress, $\overline{\rho u' w'}$ for the case shown in Figure 6 for the periods of 4 days 14–15 h. The profiles are shown every 20 min with the order of the solid, long-dashed, short-dashed, and chain-dashed curves.

Thermodynamic forcing by convection can be summarized by the so-called apparent heat source, Q_1, and moisture sink, Q_2 [cf. *Yanai et al.*, 1973]. They are, respectively, defined as source and sink terms that appear when the system is described under a moving frame of a synoptic flow. The time height section of Q_1 and Q_2, derived from TWP-ICE observations [cf. *Fridlind et al.*, 2012; *Davies et al.*, 2013], are shown in Figures 3b and 3c, respectively. Their vertical profiles are also shown for the three subperiods in Figures 4a and 4b. The most notable is strong convective forcing during the first subperiod (days 0–6) with heating and drying rates exceeding 15 K/day and 30 K/day, respectively. The convective forcing for this subperiod far exceeds

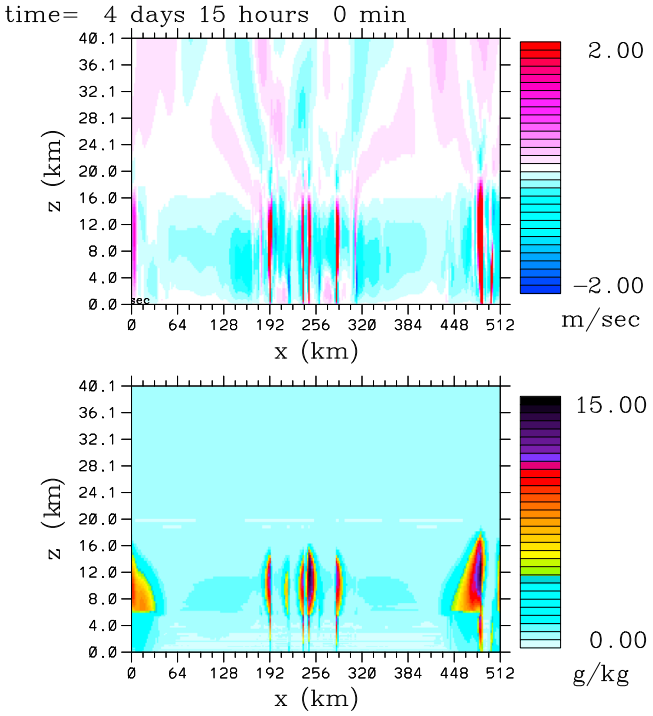

Figure 8. An example of simulated convectively generated gravity waves by a full-resolution version of NAM-SCA but with no background zonal wind. The other parameters are the same as in Figure 5: (top) the vertical velocity and (bottom) the total condensate at 4 days 14 h 40 min of the simulation.

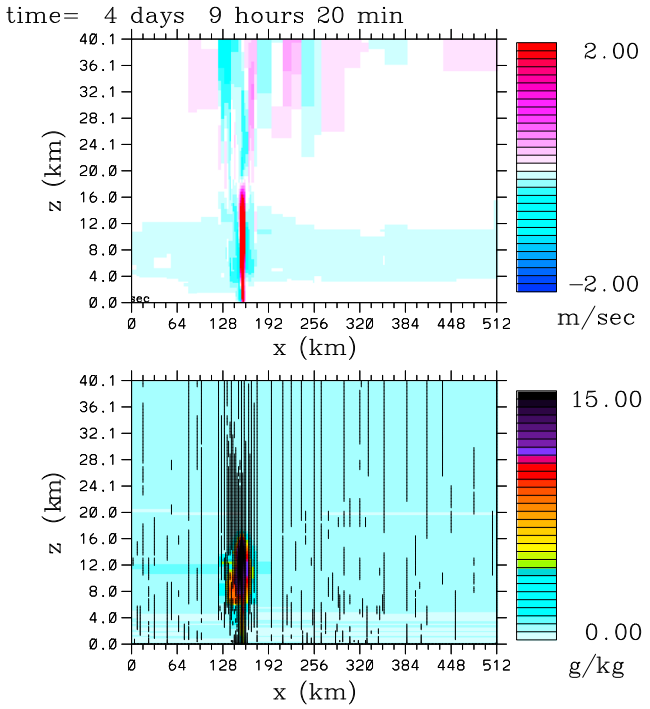

Figure 9. An example of simulated convectively generated gravity waves by NAM-SCA with the standard compression ($\gamma = 1$) and with no background zonal wind: (top) the vertical velocity and (bottom) the total condensate at 4 days 14 h 40 min of the simulation. Both model parameters and setup of the graphics are, otherwise, the same as in Figure 6.

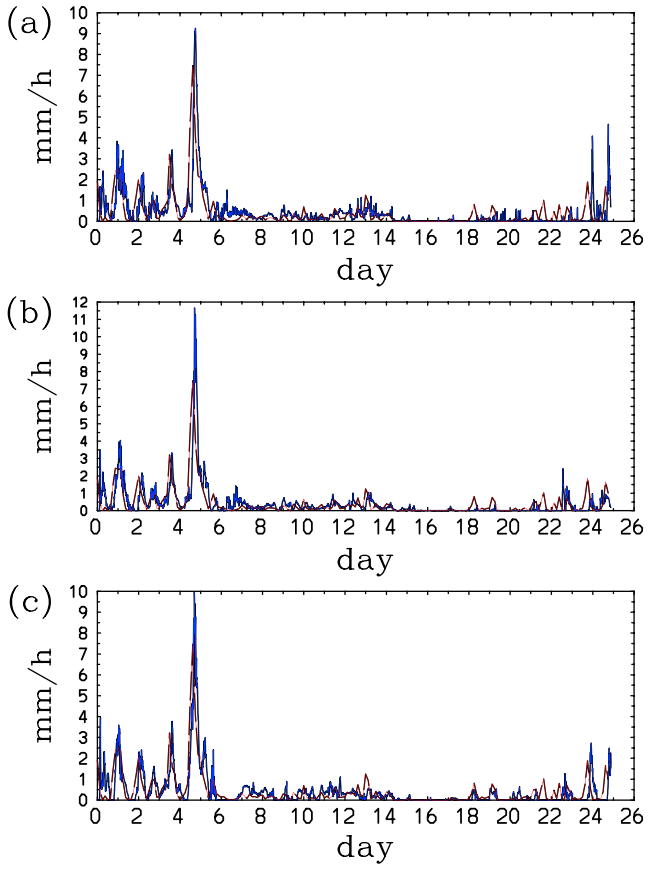

Figure 10. The simulated precipitation time series (blue) for increasing compression thresholds with $z_{2,R} = 60$ km: (a) full resolution, (b) $\gamma = 1$, and (c) $\gamma = 5$. The observed precipitation time series is superposed in red. No background zonal wind is imposed in these runs.

typical values (5 K/day) found with maritime tropical convection, as summarized in, e.g., Figure 8 of *Thompson et al.* [1979].

5. Snapshots From NAM-SCA Simulations

Without compression ($\gamma = 0$), i.e., running under full resolution everywhere, NAM-SCA reduces to a standard CRM under a finite-volume formulation. An example of convectively generated gravity waves under full resolution is shown in Figure 5: a moment that the strongest convective event of the period just begins to develop (cf. Figure 3). A well-developed convective tower to the right of the domain generates extensive gravity waves upward.

Lines of constant vertical velocity (or simply phase lines) expand radially from the cloud top, with stronger amplitude to the east of convection. According to linear gravity wave theory, the gravity wave energies are radiated radially along these phase lines. The simulated magnitudes (variances) for both horizontal and vertical winds associated with gravity waves are comparable to those estimated from radiosonde data [*Lane et al.*, 2003; *Hankinson et al.*, 2014b] and many other studies using traditional CRMs. Note that the scale for vertical velocity (Figure 5, top) is chosen relatively low so that the gravity waves can be seen clearly. The maximum vertical velocity associated with convection, 14.2 m/s, though not seen in the figure, is comparable to observations [e.g., *Collis et al.*, 2013].

Figure 6 shows a similar period, when the deepest convection is slightly more developed, for a simulation with a standard compression ($\gamma = 1$). Distribution of finite-volume segments is shown in Figure 6 (bottom) by the vertical solid lines. A convective tower topped by a stratiform cloud is well represented by a dense distribution of segments, but their distribution is much more sparse outside the cloud, except for just above

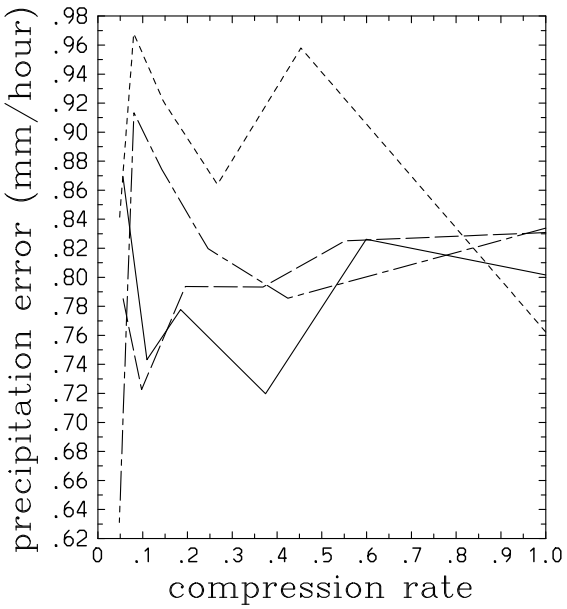

Figure 11. The root-mean-square (RMS) error for the simulated precipitation time series against the observation as a function of the compression rate. The cases are as follows: (i) with no background zonal wind with $z_{2,R} = 60$ km (solid curve) and $z_{2,R} = 45$ km (long-dash curve) and (ii) with background zonal wind with $z_{2,R} = 60$ km (short-dash curve) and $z_{2,R} = 45$ km (chain-dash curve). The cases with the background zonal wind are discussed in section 7.

convection for resolving gravity waves. Though generated gravity waves are "digitalized" compared to the full-resolution case, the overall spatial pattern and amplitude are similar. The maximum vertical velocity for this case is 13.0 m/s.

A series of instantaneous vertical profiles of the domain-averaged Reynolds stress, $\overline{\rho u' w'}$, is plotted in Figure 7 for further characterizing the generated gravity waves. The Reynolds stress decreases above the convective layer ($z \sim 15$ km), as the gravity waves propagate upward into the stratosphere. Within the sponge layer, $z > 25$ km, the Reynolds stress decays to 0 well before the uppermost boundary of the model, which suggests that the sponge layer is effective at damping the waves.

A series of experiments without the observed zonal wind is also performed in order to isolate the role of the background wind shear. Figures 8 and 9 show the same as Figures 5 and 6, respectively, but for zero mean zonal wind. Qualitatively similar results, compared to the two preceding figures, are obtained from this new simulation except the gravity waves are radiated upward in a more symmetric manner due to the absence of the background wind (Figure 8). Note that the visible asymmetry seen in the case with compression (Figure 9) is a transient feature and not a systematic property of this simulation.

6. Compressibility of NAM-SCA: With No Background Zonal Wind

In this section we consider the case with no background zonal wind and its compressibility under NAM-SCA. This simplification excludes the possibility of wind shear instability and additional wave filtering. With the domain-mean Doppler shift effect also removed, the spectrum of Reynolds stress becomes symmetric around the zero phase velocity, which significantly simplifies the interpretations.

Somewhat surprisingly, the observed precipitation time series is reproduced well when the background zonal wind is removed. Figure 10 shows the simulated precipitation time series (blue) for increasing compression (increasing γ: with $z_{2,R} = 60$ km) with the full-resolution case ($\gamma = 0$) (Figure 10a). The cases with the compression thresholds $\gamma = 1$ (Figure 10b) and $\gamma = 5$ (Figure 10c) approximately correspond to the compression rates 0.2 and 0.05, respectively (cf. section 3.2). The observed precipitation time series is superposed by the red curve (see also Figure 3a). Deterioration of the precipitation time series with increasing compression (increasing γ) is rather slow. The solid curve in Figure 11 further shows the root-mean-square (RMS) error between the simulated and observed precipitation as a function of the compression rate (by varying γ). The same measure using $z_{2,R} = 45$ km is shown by a long-dash curve.

Time height section of the apparent heat source, Q_1, and the apparent moisture sink, Q_2 are also shown in Figures 12a and 12b, respectively, for the same three cases for comparison with the observations (Figures 3b and 3c). The full-resolution case (top) demonstrates again that the wind shear is *not* critical in order to simulate convective thermodynamic feedback [cf. *Yano et al.*, 2012a, Figures 9 and 10]. The following two rows demonstrate that convective thermodynamic feedback can be relatively well simulated even with compressions rates as small as 0.05 ($\gamma = 5$). The solid curve in Figure 13 further shows the RMS errors (with the case with $z_{2,R} = 45$ km also shown by a long-dash curve). The sudden increase of errors below the 0.1 compression rate is comparable to the results in *Yano et al.* [2010].

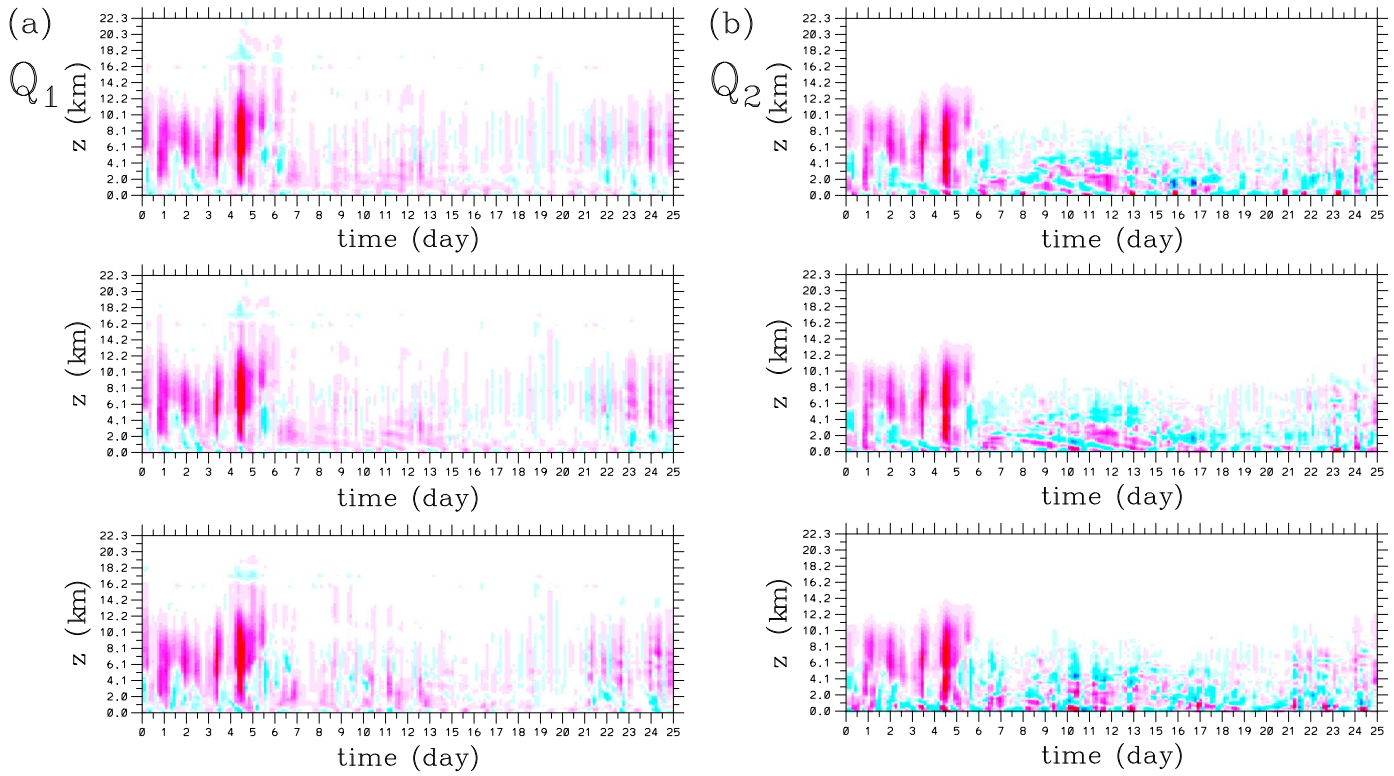

Figure 12. The time height section of (a) apparent heat source, Q_1, and (b) apparent moisture sink, Q_2, with $z_{2,R} = 60$ km. (top to bottom) With full resolution, $\gamma = 1$, and $\gamma = 5$. No background zonal wind is imposed in these runs. The values are shown for the range of −50 K/day to 50 K/day by the tones of blue (lowest) to red (highest) with the white corresponding to the zero value. Refer to Figure 3 for the color bar.

A time height section of the Reynolds stress for these three cases with $z_{2,R} = 60$ km is shown in Figure 14. High Reynolds stress events simulated by the full-resolution run (Figure 14a) are relatively well reproduced by the compressed cases (Figures 14a and 14b). The same is seen in the case with $z_{2,R} = 45$ km (not shown). The sign of the net Reynolds stress is arbitrarily selected by slight asymmetries under the absence of the background wind, and so different cases should not necessarily correspond in terms of the sign. The Reynolds stress field gets noisier with decreasing compression rates (cf. Figure 17 below). Figure 15 shows the RMS difference of the absolute Reynolds stress between the compressed and the full-resolution results by solid and long-dash curves, respectively, for $z_{2,R} = 60$ km and 45 km, both of which show that the difference increases slowly with reduced compression rate.

Figure 16 shows the Reynolds stress as a function of horizontal phase velocity at $z = 20$ km. The vertical height is chosen high enough so that no gravity wave source is expected above and low enough so that the effects of the sponge layer are not felt. Here the Reynolds stress is calculated from the cospectrum, defined by $Re(\rho\hat{u}\hat{w}^*)$, where $\hat{u}$ and $\hat{w}$ are the Fourier transform of u' and w' in time and horizontal directions; "$*$" designates a complex conjugate. The cospectrum is integrated in the wave number, k, and the frequency, ω, domain over 2 m/s phase velocity ($c_p = \omega/k$) bins. The cospectrum density is normalized so that the integral of the spectra shown in Figure 16 over c_p is equal to the net Reynolds stress.

With no background wind, linear theory suggests that upward propagating gravity waves have positive Reynolds stress for the positive phase velocity ($c_p > 0$) and negative Reynolds stress for negative phase velocity ($c_p < 0$). Thus, if the Reynolds stress is ever the opposite sign to the phase velocity, this suggests downward propagating waves that may arise from a reflection from the top boundary. For each phase speed the net Reynolds stress is the same sign as the phase speed, suggesting no such spurious reflections occur in these simulations and that the sponge layers are effective.

The magnitude of the Reynolds stress monotonically increases as the phase velocity asymptotically approaches zero. This is a striking difference from the result by *Lane and Moncrieff* [2008] who also examine

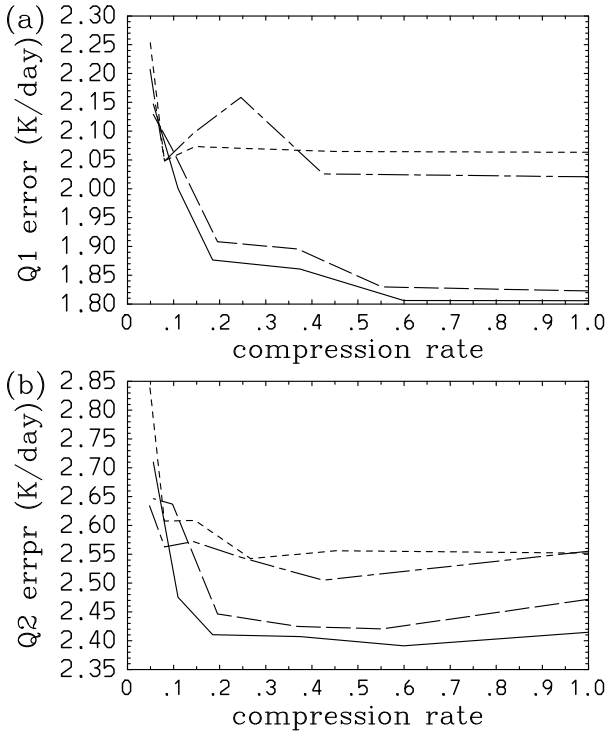

Figure 13. The root-mean-square (RMS) errors between the simulated (a) apparent heat source, Q_1, and (b) apparent moisture sink, Q_2, and the observations as functions of the compression rate. The cases are as follows: (i) with no background zonal wind with $z_{2,R} = 60$ km (solid curve) and $z_{2,R} = 45$ km (long-dash curve) and (ii) with background zonal wind with $z_{2,R} = 60$ km (short-dash curve) and $z_{2,R} = 45$ km (chain-dash curve). The cases with the background zonal wind are discussed in section 7. Note that RMS errors are given under density-weighted vertical average.

the Reynolds stress spectra for the cases with no background wind (see their Figures 9, 12) and found a spectral peak at a finite phase speed (±5–10 m/s). We interpret that our result is due to lack of horizontal diffusion (both implicit and explicit) under a finite-volume formulation. The same result is not obtained under conventional finite differences because the inherent horizontal diffusion damps gravity waves near the zero phase velocity, which might lead to an artificial peak. This interpretation is supported by Figure 12 of *Lane and Moncrieff* [2008], which shows that the peak moves to lower phase velocities with increasing horizontal resolutions.

The domain size of the simulations may furthermore contribute to the differences between our simulation and those reported by *Lane and Moncrieff* [2008]. Their much larger domain (4000 km), even without externally prescribing a wind shear, could simulate self-organization of convective systems associated with a locally induced wind shear. Such convective organization and the associated organized circulations could also modify the Reynolds stress locally through additional wave filtering, leading to an erosion of the spectrum at the lowest phase speeds. Our relatively small domain (512 km in the present study) does not allow convective self-organization.

Figure 16 also shows the results with the compression thresholds $\gamma = 0.2$ (long dash), 0.5 (short dash), 2 (chain dash), and 5 (double chain dash). Deterioration of the Reynolds stress spectrum with decreasing compression rates is slow, and overall all the curves superpose well. Thus, NAM-SCA compresses well for representing gravity waves with no background wind, although the Reynolds stress at high phase speeds increases notably with decreasing compression rates. The time-averaged total positive contribution of Reynolds stress at the height $z = 20$ km as a function of the compression rate (Figure 17) shows that there is relatively little change in the Reynolds stress for compression rates greater than about 0.6. For smaller compression rates, the Reynolds stress actually increases as compression is enhanced (γ is increased).

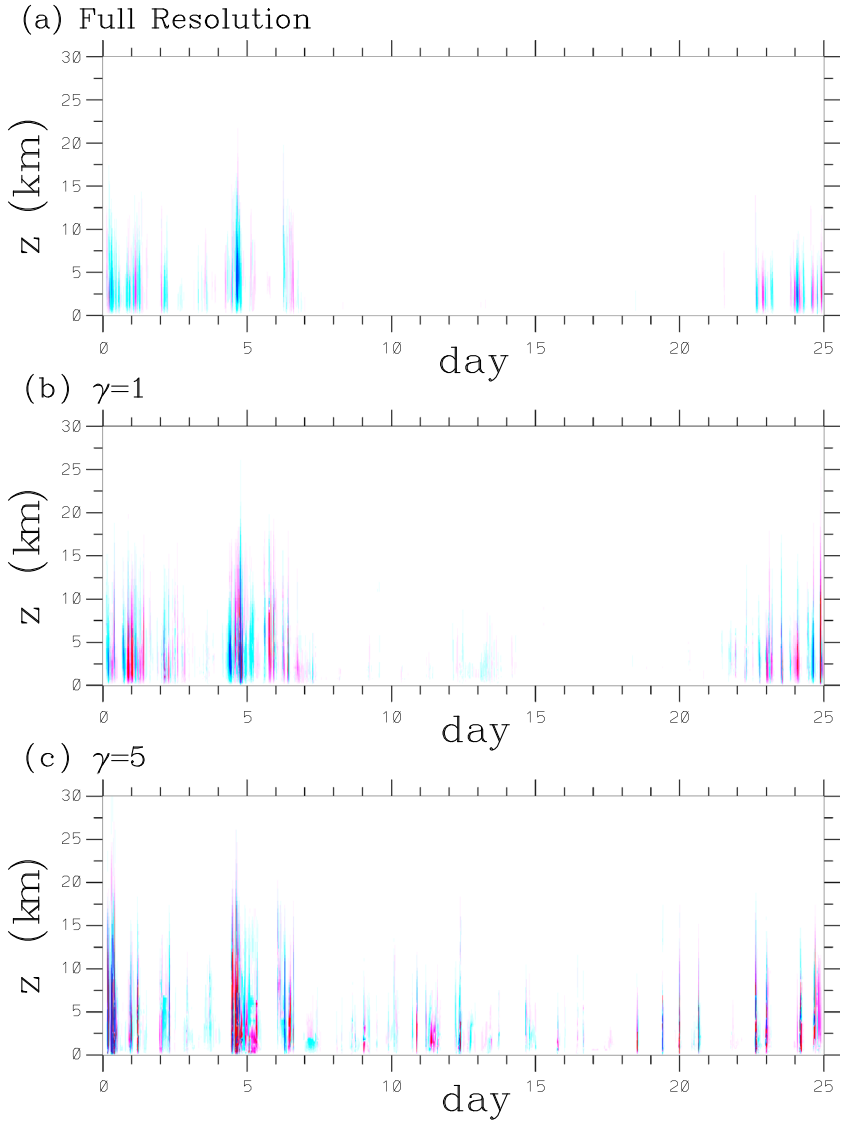

Figure 14. The time height section of the Reynolds stress for the cases with $z_{2,R}$ = 60 km: (a) full resolution, (b) γ = 1, and (c) γ = 5. No background zonal wind is imposed in these runs. The values are shown for the range of −0.02 N/m^2 to 0.02 N/m^2 by the tones of blue (lowest) to red (highest) with the white corresponding to the zero value.

In order to understand this unintuitive tendency of increased Reynolds stress with increased compression, the wave number frequency spectrum of the Reynolds stress, $Re(\rho\hat{u}\hat{w}^*)$, is examined in Figure 18 for the full-resolution case (Figure 18a) and with increasing compression (i.e., increasing compression thresholds: Figures 18b–18d). The distribution of the power does not change much in the wave number direction as compression is increased, whereas it increases substantially for the higher frequencies. The latter tendency is essentially due to more noise in simulations with increasing compressions. Specifically, a higher compression threshold, γ, makes the dynamic adaption (activation-deactivation [*Yano et al.*, 2010]) harder to happen and more abrupt when it does happen. Consequently, spurious higher-frequency gravity waves (or noise) are generated during the activation-deactivation grid adaptations. Though such an overestimation of the highest frequency gravity waves is unfavorable, especially because they are spurious, it will be shown in the next section that these spurious gravity waves are suppressed in cases with a realistic background flow by wave filtering.

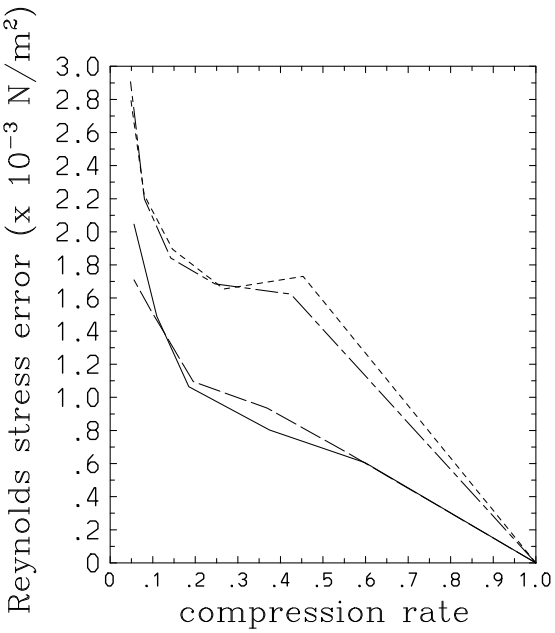

Figure 15. The root-mean-square (RMS) difference between the simulated Reynolds stress and the corresponding full-resolved cases as functions of the compression rate. The cases are as follows: (i) with no background zonal wind with $z_{2,R} = 60$ km (solid curve) and $z_{2,R} = 45$ km (long-dash curve) and (ii) with background zonal wind with $z_{2,R} = 60$ km (short-dash curve) and $z_{2,R} = 45$ km (chain-dash curve). The cases with the background zonal wind are discussed in section 7. The RMS errors are calculated as a vertical average. For the cases with no background zonal wind, the errors are measured in terms of the absolute values.

7. Compressibility of NAM-SCA: With Background Zonal Wind

In this section, the NAM-SCA simulation using the time-varying TWP-ICE wind profile is examined in terms of its ability to simulate gravity waves under compression. First, consider the model performance in comparison to observations: in general, somewhat unexpectedly the introduction of observed background zonal wind does not reduce the errors but actually increases them for some compression values. However, these changes are not dramatic, as shown by short-dash and chain-dash curves for $z_{2,R} = 60$ km and 45 km, respectively, in Figures 11 and 13. Moreover, the cases with zonal wind show larger Reynolds stress sensitivity to compression (Figure 15). These changes in errors aside, the largest influence of the change in zonal wind is on the gravity wave generation and propagation, making it an important case to consider further.

Examples of time height section of the Reynolds stress are shown in Figure 19. High Reynolds stress events simulated by the full-resolution run (top) are relatively well reproduced by the compressed cases (the two plots below), even when the system is compressed down to 0.05 (with $\gamma = 5$, bottom). In this case there is overall agreement of the signs of the Reynolds stress, which is expected because the background winds (and shear) help to shape the spectrum and bias it toward one propagation direction (see below). Note also that the overall gravity wave amplitude increases by a factor of 5 with background winds compared to the case with no wind (the scale in Figure 19 is different from that in Figure 14).

The change of the Reynolds stress spectrum with the introduction of background wind and enhanced compression (decreasing compression rates) is shown in Figure 20. Linear theory states that for upward propagating waves, the Reynold stress, $\rho u'w'$, should be the same sign as the Doppler-shifted phase velocity, e.g., as shown by Figure 7 of *Beres et al.* [2002]. The mean background zonal wind during the TWP-ICE period is about −20 m/s (cf. Figure 2) at the top of the troposphere (18 km). Thus, the −20 m/s phase velocity corresponds to the zero Doppler-shifted phase velocity when the gravity waves are generated by convection close to the tropopause. Indeed, the Reynolds stress spectrum is negative and positive, respectively, below and above −20 m/s phase velocity in Figure 20.

As compression is enhanced (γ is increased), the overall amplitude of Reynolds stress also decreases but at a rate much slower than the rate of change of compression. Note that the approximate compression rates for the given compression thresholds are 0.45 ($\gamma = 0.2$), 0.3 ($\gamma = 0.5$), 0.15 ($\gamma = 1$), 0.1 ($\gamma = 2$), and 0.05 ($\gamma = 5$). Interestingly, the peak amplitude increases from the full-resolution case to the half-compression case (with $\gamma = 0.2$) both for $z_2 = 60$ km and 45 km. However, above this compression threshold the peak decreases. The change in the Reynolds stress with compression occurs differently in different parts of the spectrum: e.g., the decrease of the peak is faster than the corresponding decrease at the faster (positive) phase speeds. Moreover, as the model is compressed down to 0.1 ($\gamma = 2$) with respect to the full model, the absolute peak decreases by about a factor of 10, whereas the tail part (for example, a local peak at $c_p = 10$ m/s) decreases only by about a quarter.

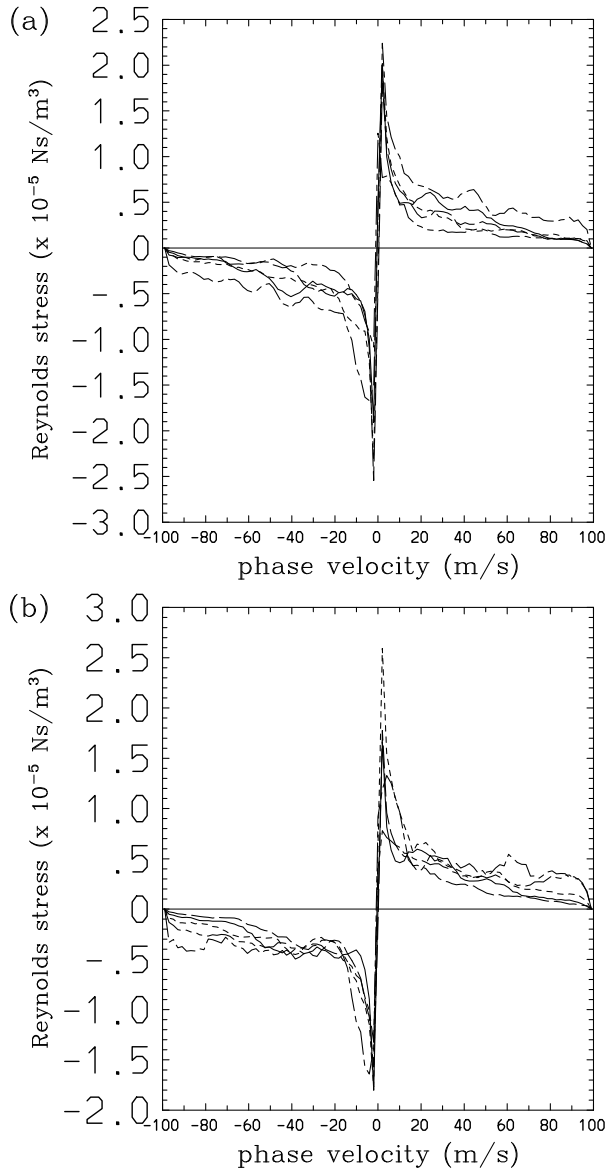

Figure 16. Reynolds stress spectrum as a function of the horizontal phase velocity measured at the height $z = 20$ km with no background zonal wind: (a) $z_{2,R} = 60$ km and (b) $z_{2,R} = 45$ km. Dependence on the compression threshold, γ, is shown: full resolution (solid curve), $\gamma = 0.2$ (long-dash curve), $\gamma = 0.5$ (short-dash curve), $\gamma = 2$ (chain-dash curve), and $\gamma = 5$ (double chain dash curve). The curves are moving averaged over five data points for the ranges of $c_p < 0$ and $c_p > 0$ separately.

The overall increase in the amplitude of the Reynolds stress spectrum as a result of adding the background winds is also seen by comparing Figure 20 with Figure 16. In particular, the peak of spectrum is increased by a factor of 10 when the background winds are added. This results in agreement with *Beres et al.* [2002], who emphasized that wind shear is important in controlling the generation and propagation of convectively generated gravity waves.

Figure 21 shows the time-averaged Reynolds stress at the height $z = 20$ km as a function of the compression rate, illustrating that the decrease of the time-averaged Reynolds stress is even slower than the changes in the peaks in the spectrum shown earlier. The reduction is less than a quarter of the full-resolution case as the model is compressed down to 0.1 ($\gamma = 2$). The time-averaged Reynolds stress actually increases when the model is initially compressed to 0.5 ($\gamma = 0.2$) from the full-resolution case with $z_2 = 60$ km.

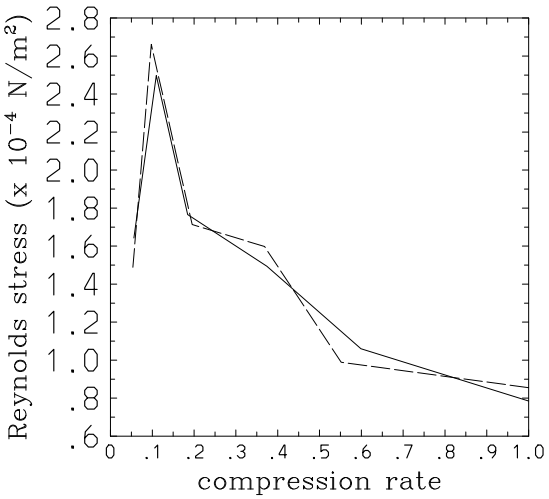

Figure 17. The time-averaged positive contribution of the Reynolds stress at the height $z = 20$ km as a function of the compression rate for the cases with $z_2 = 60$ km (solid curve) and 45 km (long-dash curve), for the case with no background zonal wind, $\bar{u} = 0$.

All these tendencies (as a result of compression) are better understood by examining the wave number frequency spectrum of the Reynolds stress (Figure 22). For the full resolution (Figure 22a), the spectrum lines, $\omega = c_p k$, with $c_p = -8$ m/s and 20 m/s, correspond to the peaks identified in Figure 20. As in the case with no wind, enhancing the compression (Figures 22b–22d) filters out the higher wave number components and generates more higher-frequency components. Namely, the compression acts as a low-pass filter in wave number space and a high-frequency noise generator at the same time. These two tendencies compensate each other, and the total Reynolds stress does not reduce significantly with enhanced compression.

These results using the observed TWP-ICE wind suggest that NAM-SCA can represent convectively generated gravity waves reasonably well. The shape of the stratospheric wave spectrum is relatively insensitive to compression, and the time-averaged Reynolds stress is even less sensitive. However, it appears that a compression rate of about 0.1 is a lower limit. Under a further compression to the rate 0.05 ($\gamma = 5$), the Reynolds stress suddenly drops to half of the full-resolution case in with $z_2 = 60$ km, making it a poor representation of the uncompressed solution.

8. Discussion

The present paper investigated the capacity of NAM-SCA [*Yano et al.*, 2010, 2012a; *Yano and Bouniol*, 2010, 2011; *Yano and Baizig*, 2012] for simulating convectively generated gravity waves. The main goal of this study was to explore the possibility of using NAM-SCA as a unified convection and gravity wave source parameterization, in the same spirit as superparameterization. For the purposes of this study NAM-SCA can be considered a truncated cloud-resolving model (CRM) and/or a fully prognostic mass flux convective parameterization. Here we specifically investigated the effects of NAM-SCA's truncation (or compression) on the representation of the spectrum of gravity waves generated by deep convection. We adopted a period from the Tropical Warm Pool-International Cloud Experiment (TWP-ICE) for investigation, and two principal cases were constructed with and without observed zonal winds under the TWP-ICE large-scale forcing. Both sets of simulations compared well to the observations.

The key question considered by this study concerns the change in the gravity waves with increased model compression (i.e., decreasing compression rates and increasing compression thresholds, γ). The net gravity wave activity was measured by the Reynolds stress just above the tropopause (20 km). In the case with no background wind the magnitude of the gravity wave activity increased by a factor of 2–3 with enhancing compression (cf. Figure 17), whereas with the inclusion of background zonal wind its magnitude varied by less than a factor of 2 with decreasing compression rates down to 0.1 ($\gamma = 2$: cf. Figure 21). Notably, the compression rate of 0.1 corresponds to about 10% of the computational expense of a traditional CRM. These results demonstrate NAM-SCA's capacity to represent convectively generated gravity waves even under a relatively strong compression.

The wave number frequency spectrum of the Reynolds stress revealed the details of the effects of model compression on the gravity waves. In the case with no background wind (Figure 18), more noise is generated in the higher frequencies with enhancing compression, leading to increasing Reynolds stress in total. This higher-frequency noise is essentially spurious gravity waves generated by the adaptive grid process. In the case with background wind (Figure 22), the spectrum is broader in wave number space under full model resolution (i.e., when there is no compression). It was shown that for this case, the enhancement of compression works as a low-pass filer that removes the higher wave number components. At the same

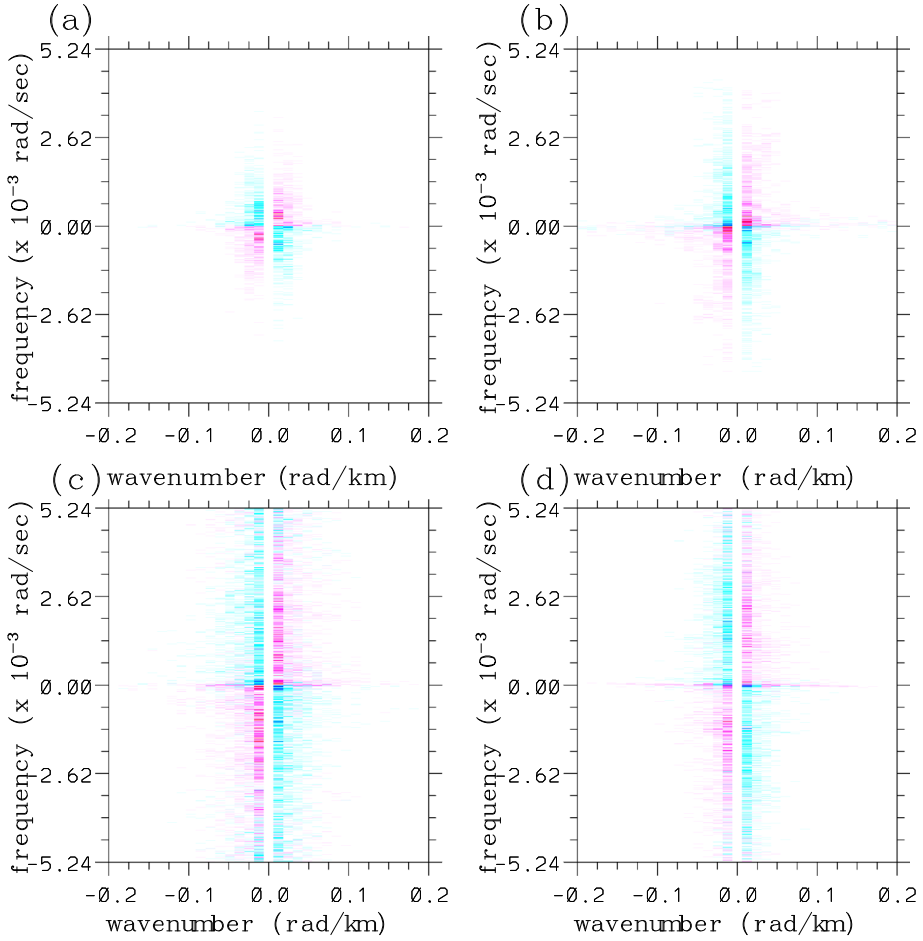

Figure 18. The wave number frequency spectrum of the Reynolds stress defined at $z = 20$ km height with the wave number and the frequency as the horizontal and the vertical axes, respectively. The cases shown are with $z_{2,R} = 60$ km and no zonal wind: (a) full resolution, (b) $\gamma = 0.5$, (c) $\gamma = 2$, and (d) $\gamma = 5$. The power spectrum of the range -10^{-6} to 10^{-6} is shown by the deepest blue (-10^{-6}) to lighter blues and then from lighter reds to the deepest red (10^{-6}) in linear scale. The white corresponds to zero power.

time, however, more higher-frequency noise is still generated under enhanced compression. The generation of these spurious high-frequency gravity waves compensated the erosion of the higher wave number components, and the total Reynolds stress was thereby approximately conserved (cf. Figure 21).

The erosion of the higher wave number components with enhancing compression is analogous to the finding by *Lane and Knievel* [2005], who showed that the higher wave number components erode with decreasing resolution in CRM simulations. Nevertheless, in NAM-SCA the erosion of the higher wave numbers by compression is much slower than what would occur with a reduction of the model resolution in a regular CRM. The similarity between the spectra of the full-resolution (Figure 18) and the 25% compression ($\gamma = 0.5$) cases (Figure 22) clearly demonstrates the strength of NAM-SCA's compression method.

The present study also has led to the following two secondary findings:

1. Both the apparent heat source and moisture sink, Q_1 and Q_2, are well simulated even without the background zonal winds. This result suggests that the wind shear may not be critical for successful parameterization of the thermodynamic effects of convection. This finding strengthens the similar conclusion made by *Yano et al.* [2012a] that mesoscale organization may not be essential for parameterization of the thermodynamic effects. However, this result clearly does not exclude the potential importance of mesoscale organization for convective momentum transport parameterization [e.g., *Moncrieff*, 1992]. This aspect warrants further investigations under NAM-SCA, especially

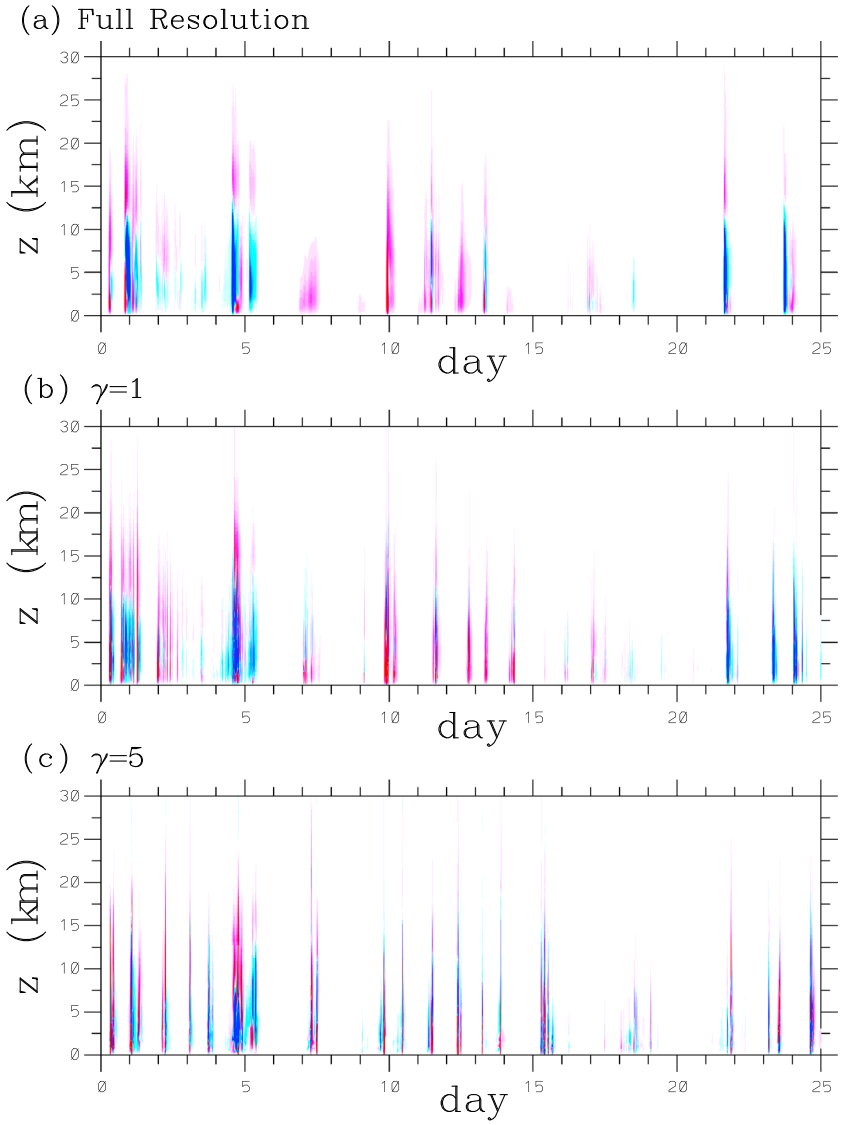

Figure 19. The same as Figure 14 but with the observed background zonal wind. The time height section of the Reynolds stress for the cases with $z_{2,R} = 60$ km: (a) full resolution, (b) $\gamma = 1$, and (c) $\gamma = 5$. The values are shown for the range of −0.1 N/m^2 to 0.1 N/m^2 by the tones of blue (lowest) to red (highest) with the white corresponding to the zero value.

considering the ubiquitous nature of multiscale convective organization [cf. *Moncrieff*, 1995, 2010; *Yano et al.*, 2012b].

2. The generation of gravity waves is enhanced in the lower stratosphere by an order of magnitude in the presence of background wind shear. Our finding suggests not only the importance of the interactions between the wind shear and convection in controlling the behavior of gravity waves (e.g., Reynolds stress) and shaping the spectrum, as emphasized by *Beres et al.* [2002], but also in defining the total amplitude. This tendency has also been documented by *Lane and Moncrieff* [2010], who identify that tilted convective updrafts of organized convection in shear lead to a more efficient wave generation process. We also speculate that wind shear locally enhanced by convective organization may induce local shear instabilities leading to enhanced generation of gravity waves from the shear zone.

The present study as a whole suggests that NAM-SCA can serve not only as a prototype for convection parameterization but also as a prototype for gravity wave parameterization. In this respect, the strength of NAM-SCA based on a direct reduction of a full physical model [cf. *Yano et al.*, 2005, see also *Yano*, 2012b] may be emphasized. Indeed, one main advantage of NAM-SCA for this purpose is that there remains

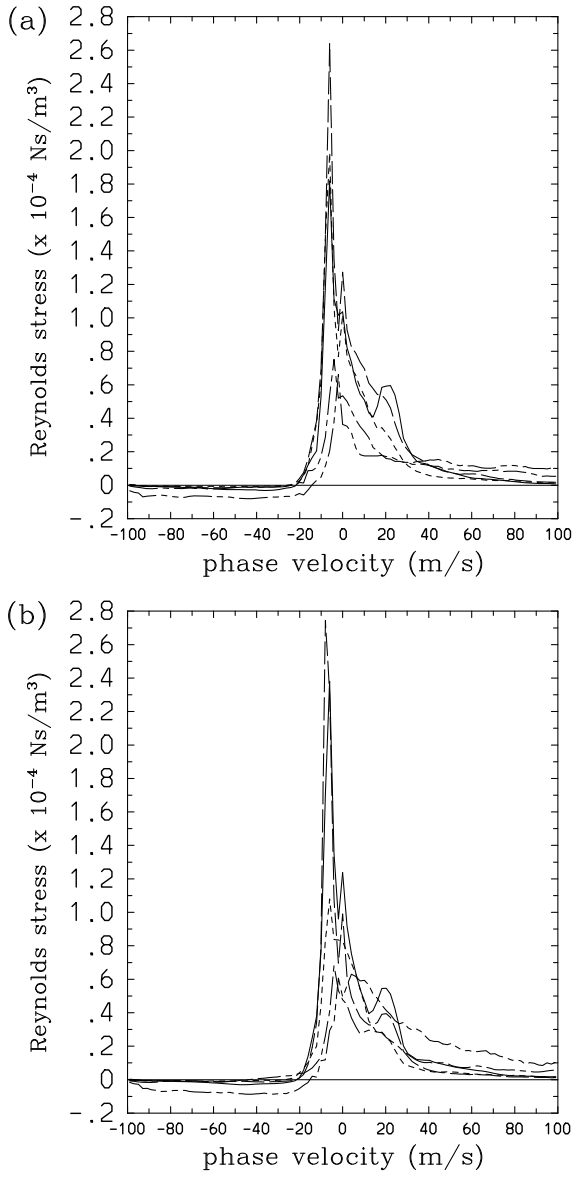

Figure 20. The same as Figure 16 but with the background zonal wind: (a) $z_{2,R} = 60$ km and (b) $z_{2,R} = 45$ km. Reynolds stress spectrum as a function of the phase velocity. Dependence on the compression threshold, γ: full resolution (solid curve), $\gamma = 0.2$ (long-dash curve), $\gamma = 0.5$ (short-dash curve), $\gamma = 2$ (chain dash curve), and $\gamma = 5$ (double chain dash curve). The curves are moving averaged over five data points for the ranges of $c_p \leq -20$ m/s and $c_p \geq 0$ m/s. The range over $-20 < c_p < 0$ m/s is not moving averaged in order to avoid erosion of the primary peak of the spectrum.

a physically consistent link between the convection and gravity waves, which is an improvement over existing approaches.

Specifically, the current approach to parameterize convective gravity waves is to relate the wave activity to the convective heating amplitude [*Beres et al.*, 2005; *Song and Chun*, 2005; *Song et al.*, 2007]. Comparing the heating rate time height section (Figure 12) with that of the gravity wave generated Reynolds stress (Figures 14 and 19) suggests that such a simple relationship does not exist, especially for the case with background winds, where the gravity waves are more equally distributed over the whole TWP-ICE period compared to convective heating, which is only dominant over the initial active period. We believe that a key wave generation process not accounted for by the diabatic heating approach is the transition of the convective updraft into an oscillatory mode as part of the overshoot into the overlying stable air (viz., the mechanical oscillator effect). This is also an obvious limitation of the conventional mass flux

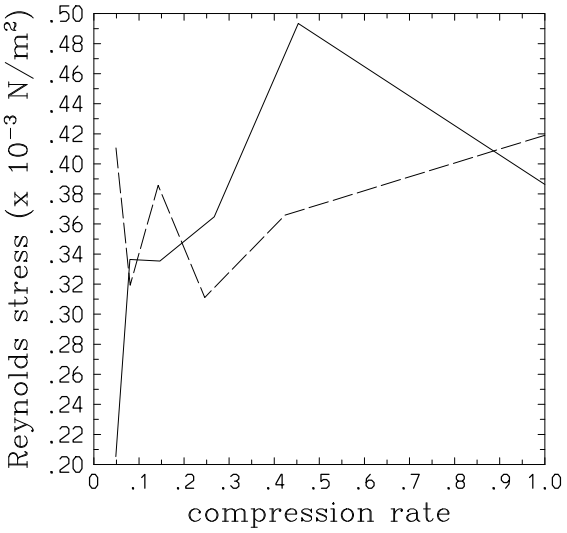

Figure 21. The time-averaged total Reynolds stress at the height $z = 20$ km as a function of the compression rate for the cases with $z_2 = 60$ km (solid curve) and 45 km (long-dash curve).

parameterization that adopts a steady plume hypothesis. By taking a fully prognostic formulation, on the other hand, NAM-SCA can naturally describe such a transition.

In terms of implementation of NAM-SCA as a convective gravity parameterization a number of practical issues would need to be addressed. The main issue concerns the parameterization of the resultant wave drag (e.g., from wave breaking). In principle, NAM-SCA could be configured with a high-enough model top and high-enough vertical resolution such that convective gravity wave drag was explicitly resolved in the middle atmosphere; tendencies could then be fed back to the parent GCM directly. However, this approach would be computationally expensive and another drag parameterization [e.g., *Alexander and Dunkerton*, 1999; *Lindzen*, 1981] would still be required for other wave sources like fronts. A simpler (and less expensive) implementation would be to use NAM-SCA purely as a source parameterization, with time-varying spectral wave properties derived from NAM-SCA as it is running. Those wave spectra would then serve as inputs to an existing wave drag parameterization that could also simultaneously treat waves from other sources.

The above suggested implementation would treat each model column separately. Such an approach, coupled with the horizontal periodicity of NAM-SCA, would prohibit gravity waves propagating between neighboring grid boxes. This column-based approach is a limitation of almost all parameterizations of convection and gravity waves. However, *Song and Chun* [2008] introduced a lagrangian wave drag parameterization (that was based on ray tracing), which allows horizontal propagation of waves beyond single-model columns. In principle, NAM-SCA could be used as an input to such a lagrangian wave drag parameterization to produce a more realistic spatial pattern of wave drag.

The present study has only considered gravity waves generated by convection, but other nonorographic sources could also be represented by NAM-SCA. For example, fronts are an important gravity wave source, but despite both observational [*Eckermann and Vincent*, 1993] and modeling [*Griffiths and Reeder*, 1996; *Reeder and Griffiths*, 1996] evidence, there has been only limited progress in the parameterization of frontal waves [e.g., *Charron and Manzini*, 2002]. NAM-SCA has the potential to represent such subgrid-scale processes; testing the performance of NAM-SCA in representing fronts and gravity waves will be a topic of future research.

The present work identifies the potential for extending the superparameterization approach to include a convective gravity wave source parameterization. This parameterization could provide physically consistent inputs to the wave drag parameterization of the parent global model. Although such an approach might be too computationally expensive under the current superparameterization framework, the use of a compressed model such as NAM-SCA would be more feasible.

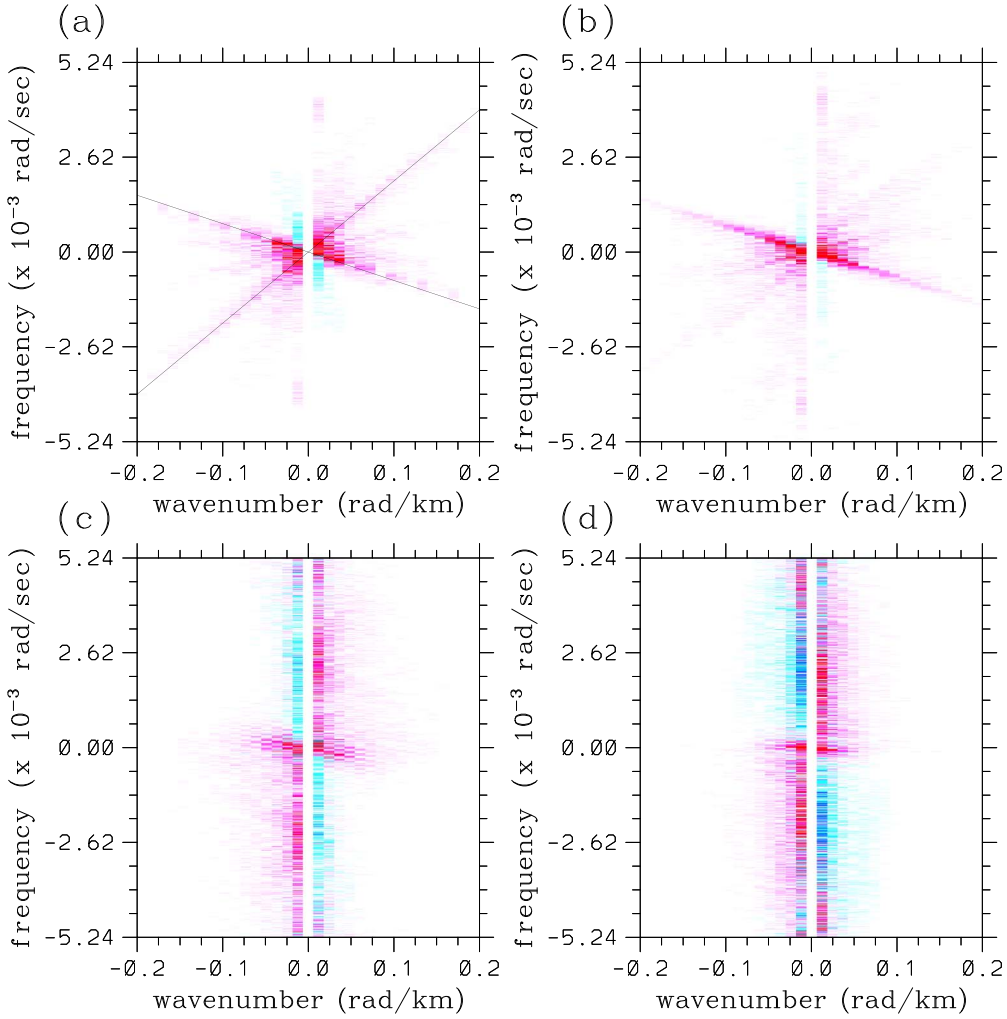

Figure 22. The wave number frequency spectrum of the Reynolds stress defined at $z = 20$ km height with the wave number and the frequency as the horizontal and the vertical axes, respectively. The cases shown are with $z_{2,R} = 60$ km and with zonal wind: (a) full resolution, (b) $\gamma = 0.5$, (c) $\gamma = 2$, and (d) $\gamma = 5$. The power spectrum of the range -10^{-6} to 10^{-6} is shown by the deepest blue (-10^{-6}) to lighter blues and then from lighter reds to the deepest red (10^{-6}) in linear scale. The white corresponds to zero power. In Figure 22a, the lines for $\omega = c_p k$ with $c_p = -8$ m/s and 20 m/s are added in order to indicate the dominant gravity wave phase velocities.

Appendix A: Model Parameters

Here the model parameters are listed with the values adopted. See *Yano et al.* [2010] for the precise definitions of the parameters.

A1. Model Resolution Related Parameters:

$L = 512$ km: horizontal domain size
$N_x = 256$: total number of volume segments under a full resolution
$M_x = 2$: minimum number of volume segments allowed at each vertical level
$\Delta t = 2$ s: time step
$\Delta X = L/2$: length of the volume segment under the minimum resolution
$\Delta x = 2$ km: full horizontal resolution

A2. Vertical Coordinate:

$H = 70$ km: model top height
$N_z = 91$: total number of full vertical levels

$\Delta z_0 = 50$ m: the highest vertical resolution at the lowest layer (full-level layer depth)
$\Delta z_n = 1000$ m: the lowest vertical resolution (full-level layer depth)

A3. Critical Vertical Levels:

$k_b = 1$: maximum full level at which the full resolution is always maintained
$k_m = 40$: top level at that the full resolution is initially introduced (5.4 km height)
$k_t = N_z$: maximum height level at which activation and deactivation of volume segments is performed. Above this level, the minimum resolution M_x is always maintained

A4. Vertical Depth for Performing Activation and Deactivation:

$\Delta k_a = 3$: vertical depth over which activation is performed
$\Delta k_d = 0$: vertical depth over which the deactivation condition is checked

A5. Intervals for Activation and Deactivation

$n_a = 10$: interval for performing activation given as a number of time steps
$n_d = 10$: interval for performing deactivation given as a number of time steps

A6. Relative Thresholds for Activation and Deactivation:

$\gamma \equiv \gamma_a = \gamma_d = 1.0$: threshold for activation and deactivation relative to the standard deviation at a given vertical level (compression threshold)
$\gamma_{\min} = 0.1$: threshold for activation and deactivation relative to the total standard deviation

A7. Parameters for the Sponge Layer:

$z_{1,R} = 25$ km: the bottom of the sponge layer: stand-alone cases
$z_{2,R} = 60$ km (by default with $z_{2,R} = 45$ km as a possible alternative): the level above which the maximum Rayleigh damping rate is imposed (defaults1)
$\tau_R = 60$ s: the maximum Rayleigh damping time scale in the sponge layer (default)

Acknowledgments
J.I.Y. notes the context of COST Action ES0905 for the present study. T.P.L. is supported by the Australian Research Council (ARC) Future Fellowships Scheme (FT0990892) and the ARC Centre of Excellence for Climate System Science (CE110001028). The authors also thank Mitch Moncrieff for constructive editorial comments and the two anonymous reviewers as well as the editorial effort by Steve Ghan.

References

Alexander, M. J., and T. J. Dunkerton (1999), A spectral parameterization of mean-flow forcing due to breaking gravity waves, *J. Atmos. Sci.*, *56*, 4167–4182.
Beres, J. H., M. J. Alexander, and J. R. Holton (2002), Effects of tropospheric wind shear on the spectrum of convectively generated gravity waves, *J. Atmos. Sci.*, *59*, 1805–1824.
Beres, J. H., R. R. Garcia, B. A. Boville, and F. Sassi (2005), Implementation of gravity wave source spectrum parameterization dependent on the properties of convection in the Whole Atmospheric Community Climate Model (WACCM), *J. Geophys. Res.*, *110*, D10108, doi:10.1029/2004JD005504.
Charron, M., and E. Manzini (2002), Gravity waves from fronts: Parameterization and middle atmosphere response in a general circulation model, *J. Atmos. Sci.*, *59*, 923–941.
Collis, S., A. Protat, P. T. May, and C. Williams (2013), Statistics of storm updraft velocities from TWP-ICE including verification with profiling measurements, *J. Appl. Meteorol. Climatol.*, *52*, 1909–1922.
Crook, N. A. (2001), Understanding hector: The dynamics of island thunderstorms, *Mon. Weather Rev.*, *129*, 1550–1563.
Davies, L., et al. (2013), A single-column model ensemble approach applied to the TWP-ICE experiment, *J. Geophys. Res. Atmos.*, *118*, 6544–6563, doi:10.1002/jgrd.50450.
Drosdowsky, W. (1996), Variability of the Australian summer monsoon at Darwin: 1957–92, *J. Clim.*, *9*, 85–96.
Eckermann, S. D., and R. A. Vincent (1993), VHF radar observations or gravity-wave production by cold fronts over southern Australia, *J. Atmos. Sci.*, *50*, 785–806.
Eckermann, S. D., et al. (2009), High-altitude data assimilation system experiments for the northern summer mesosphere season of 2007, *J. Atmos. Sol. Terr. Phys.*, *71*, 531–551.
Fovell, R., D. Durran, and J. R. Holton (1992), Numerical simulation of convectively generated stratospheric gravity waves, *J. Atmos. Sci.*, *49*, 1427–1442.
Fridlind, A. M., et al. (2012), A comparison of TWP-ICE observational data with cloud-resolving model results, *J. Geophys. Res.*, *117*, D05204, doi:10.1029/2011JD016595.
Fritts, D. C., and M. J. Alexander (2003), Gravity wave dynamics and effects in the middle atmosphere, *Rev. Geophys.*, *41*, 1003, doi:10.1029/2001RG000106.
Godunov, S. K. (1959), A difference scheme for numerical computation of discontinuous solutions of equations in fluid mechanics, *Math Sbornik*, *47*, 271–306.
Grabowski, W. W., and P. K. Smolarkiewicz (1999), CRCP: A cloud resolving convection parameterization for modeling the tropical convective atmosphere, *Physica D*, *133*, 171–178.
Griffiths, M., and M. J. Reeder (1996), Stratospheric inertial-gravity waves generated in a numerical model of frontgenesis. I: Model simulations, *Q. J. R. Meteorol. Soc.*, *122*, 1153–1174.
Hankinson, C. M., M. J. Reeder, and T. P. Lane (2014a), Gravity waves generated by convection during TWP-ICE. Part I: Inertia-gravity waves, *J. Geophys. Res. Atmos.*, *119*, doi:10.1002/2013JD020724.
Hankinson, C. M., M. J. Reeder, and T. P. Lane (2014b), Gravity waves generated by convection during TWP-ICE. Part II: High-frequency gravity waves, *J. Geophys. Res. Atmos.*, *119*, doi:10.1002/2013JD020726.
Holton, J. R., and M. J. Alexander (1999), Gravity waves in the mesosphere generated by tropospheric convection, *Tellus*, *51A*, 45–58.
Holton, J. R., J. H. Beres, and X. Zhou (2002), On the vertical scale of gravity waves excited by localized thermal forcing, *J. Atmos. Sci.*, *59*, 2019–2023.

Kiehl, J. T., J. J. Hack, and B. P. Briegleb (1994), The simulated Earth radiation budget of the National Center for Atmospheric Research community climate model CCM2 and comparisons with the Earth Radiation Budget Experiment (ERBE), *J. Geophys. Res.*, *99*, 20,815–20,827.

Khairoutdinov, M., C. DeMott, and D. Randall (2008), Evaluation of the simulated interannual and subseasonal variability in an AMIP-style simulation using the CSU multiscale modelling framework, *J. Clim.*, *21*, 413–431.

Lane, T. P., and J. C. Knievel (2005), Some effect of model resolution on simulated gravity waves generated by deep mesoscale convection, *J. Atmos. Sci.*, *62*, 3408–3419.

Lane, T. P., and M. W. Moncrieff (2008), Stratospheric gravity waves generated by multiscale tropical convection, *J. Atmos. Sci.*, *65*, 2598–2614.

Lane, T. P., and M. W. Moncrieff (2010), Characterization of momentum transport associated with organized moist convection and gravity waves, *J. Atmos. Sci.*, *67*, 3208–3225.

Lane, T. P., and M. J. Reeder (2001), Convectively generated gravity waves and their effect on the cloud environment, *J. Atmos. Sci.*, *58*, 2427–2440.

Lane, T. P., M. J. Reeder, and T. L. Clark (2001), Numerical modeling of gravity wave generation by deep tropical convection, *J. Atmos. Sci.*, *58*, 1249–1274.

Lane, T. P., M. J. Reeder, and F. M. Guest (2003), Convectively generated gravity waves observed from radiosonde data taken during MCTEX, *Q. J. R. Meteorol. Soc.*, *129*, 1731–1740.

LeVeque, R. J. (2002), *Finite Volume Methods for Hyperbolic Problems*, 578 pp., Cambridge Univ. Press, Cambridge.

Lindzen, R. S. (1981), Turbulence and stress due to gravity wave and tidal breakdown, *J. Geophys. Res.*, *86*, 9701–9714.

Mallat, S. (1998), *A Wavelet Tour of Signal Processing,* 2nd ed., 637 pp., Academic Press, San Diego, Calif.

May, P. T., J. H. Mather, G. Vaughan, K. N. Bower, C. Jakob, G. M. McFarquhar, and G. G. Mace (2008), The Tropical Warm Pool International Cloud Experiment, *Bull. Am. Meteorol. Soc.*, *89*, 629–645.

Moncrieff, M. W. (1992), Organized convective systems—Archetypal dynamic-models, mass and momentum flux theory, and parametrization, *Q. J. R. Meteorol. Soc.*, *507*, 819–850.

Moncrieff, M. W. (1995), Mesoscale convection from a large-scale perspective, *Atmos. Res.*, *35*, 87–112.

Moncrieff, M. W. (2010), The multiscale organization of convection at the interaction of weather and climate, *Why Climate Vary?, Geophys. Monogr. Ser.,* vol. 189, edited by D.-Z. Sun and F. Bryan, pp. 3–26, AGU, Washington, D. C., doi:10.1029/2008GM000838.

Piani, C., D. Durran, M. J. Alexander, and J. R. Holton (2000), A numerical study of three-dimensional gravity waves triggered by deep tropical convection and their role in the dynamics of the QBO, *J. Atmos. Sci.*, *57*, 3689–3702.

Randall, D. A., M. Khairoutdinov, A. Arakawa, and W. Grabowski (2003), Breaking the cloud parameterization deadlock, *Bull. Am. Meteorol. Soc.*, *84*, 1547–1564.

Reeder, M. J., and M. Griffiths (1996), Stratospheric inertial-gravity waves generated in a numerical model of frontgenesis. II: Wave sources, generation mechanism and momentum fluxes, *Q. J. R. Meteorol. Soc.*, *122*, 1175–1195.

Song, I.-S., and H.-Y. Chun (2005), Momentum flux spectrum of convective forced internal gravity waves and its application to gravity wave drag aparameterization. Part I: Theory, *J. Atmos. Sci.*, *62*, 107–124.

Song, I.-S., and H.-Y. Chun (2008), A lagrangian spectral parameterization of gravity wave drag induced by cumulus convection, *J. Atmos. Sci.*, *65*, 1204–1224.

Song, I.-S., H.-Y. Chun, and T. P. Lane (2003), Generation mechanisms of convectively forced internal gravity waves and their propagation to the stratosphere, *J. Atmos. Sci.*, *60*, 1960–1980.

Song, I.-S., H.-Y. Chun, R. R. Garcia, and B. A. Boville (2007), Momentum flux spectrum of convectively forced internal gravity waves and its application to gravity wave drag parameterization. Part II: Impacts in a GCM (WACCM), *J. Atmos. Sci.*, *64*, 2286–2308.

Thompson Jr., R. M., S. W. Payne, E. E. Recker, and R. J. Reed (1979), Structure and properties of synoptic-scale wave disturbances in the intertropical convergence zone of eastern Atlantic, *J. Atmos. Sci.*, *36*, 53–72.

Warner, C. D., and M. E. McIntyre (2001), An ultrasimple spectral parameterization for nonorographic gravity waves, *J. Atmos. Sci.*, *58*, 1837–1857.

Yanai, M. S., S. Esbensen, and J. H. Chu (1973), Determination of bulk properties of tropical cloud clusters from large-scale heat and moisture budgets, *J. Atmos. Sci.*, *30*, 611–627.

Yano, J.-I. (2010), Downscaling, parameterization, decomposition, compression: A perspective from the multiresolutional analysis, *Adv. Geophy.*, *23*, 65–71.

Yano, J.-I. (2012a), Mass-flux subgrid-scale parameterization in analogy with multi-component flows: A formulation towards scale independence, *Geosci. Model Dev.*, *5*, 1425–2440.

Yano, J.-I. (2012b), Comments on "A density current parameterization coupled with Emanuel's convection scheme. Part I: The models", *J. Atmos. Sci.*, *69*, 2083–2089.

Yano, J.-I., and H. Baizig (2012), Single SCA-plume dynamics, *Dyn. Atmos. Oceans*, *58*, 62–94.

Yano, J.-I., and D. Bouniol (2010), A minimum bulk microphysics, *Atmos. Chem. Phys. Discuss.*, *10*, 30,305–30,345, doi:10.5194/acpd-10-30305-2010.

Yano, J.-I., and D. Bouniol (2011), Interactive comment on "A minimum bulk microphysics", *Atmos. Chem. Phys. Discuss.*, *10*, C14,638–C14,654. [Available at www.atmos-chem-phys-discuss.net/10/C14638/2011/.]

Yano, J.-I., J.-L. Redelsperger, F. Guichard, and P. Bechtold (2005), Mode decomposition as a methodology for developing convective-scale representations in global models, *Q. J. R. Meteorol. Soc.*, *131*, 2313–2336.

Yano, J.-I., P. Benard, F. Couvreux, and A. Lahellec (2010), NAM-SCA: Nonhydrostatic anelastic model under segmentally constant approximation, *Mon. Weather Rev.*, *138*, 1957–1974.

Yano, J.-I., S. K. Cheedela, and G. L. Roff (2012a), Towards compressed super-parameterization: Test of NAM-SCA under single-column GCM configurations, *Atmos. Chem. Phys. Discuss.*, *12*, 28,237–28,303.

Yano, J.-I., C. Liu, and M. W. Moncrieff (2012b), Atmospheric convective organization: Homeostasis or self-organized criticality?, *J. Atmos. Sci.*, *69*, 3449–3462.